RSC Advances

ROYAL SOCIETY OF CHEMISTRY

www.rsc.org/advances

Synthesis of one-dimensional $Bi_2O_2CO_3$-$Bi(OHC_2O_4)$•$2H_2O$ heterojunctions with excellent adsorptive and photocatalytic performance

Yin Peng*[a], Ke Ke Wang[a], Pian-Pian Yu[a], Ting Liu[a], An Wu Xu*[b]

Receipt/Acceptance Data [DO NOT ALTER/DELETE THIS TEXT]
Publication data [DO NOT ALTER/DELETE THIS TEXT]
DOI: 10.1039/b000000x [DO NOT ALTER/DELETE THIS TEXT]

One-dimensional (1D) $Bi_2O_2CO_3$-$Bi(OHC_2O_4)$•$2H_2O$ heterostructure was synthesized by low temperature solution method using $Bi(OHC_2O_4)$•$2H_2O$ nanorods as template. $Bi_2O_2CO_3$ nanosheets vertically grew onto the $Bi(OHC_2O_4)$•$2H_2O$ rods along the long axial direction. Its adsorption capacity for organic pollutants was evaluated using methyl orange (MO) as model. The results showed that $Bi_2O_2CO_3$-$Bi(OHC_2O_4)$•$2H_2O$ heterostructure had excellent adsorption capacity of 95.78 mg/g and repeatability for MO. $Bi_2O_2CO_3$-$Bi(OHC_2O_4)$•$2H_2O$ heterostructure also possessed excellent photocatalytic activity to degrade dyes (MO, RhB and MB) under solar/UV light irradiation. 20 mg/L of RhB, 30 mg/L of MB and 75 mg/L of MO could be completely degraded by $Bi_2O_2CO_3$-$Bi(OHC_2O_4)$•$2H_2O$ photocatalyst in 15, 25 and 120 min, respectively. This superior adsorptive and photocatalytic performance is ascribed to the synergistic effect of big BET surface area and the formation of numbers of junctions in $Bi_2O_2CO_3$-$Bi(OHC_2O_4)$•$2H_2O$ heterostructure. The trapping experiment of active species during the photocatalytic degradation was carried out, and the result indicates that $O_2^{\bullet-}$ radical and h^+ play a major role in the photocatalytic degradation process. This study provides a general and effective method to fabricate unique 1D $Bi_2O_2CO_3$-$Bi(OHC_2O_4)$•$2H_2O$ heterostructure with both photocatalytic and adsorptive performance on a large scale.

Introduction

While incredible strides in science and technology have indeed raised the quality and standard of the human life and health, it has nevertheless brought about a multitude of problems as well. Nowadays, organic dyes are used for coloring in a wide range of industries, such as textiles, dying, leather, paper and other industries due to the rapid development of the industrialized global economy.[1] Unfortunately, the synthetic origin and complex aromatic molecular structures of the pollutants in color wastewater make these dyes more stable and resistant to biodegradation, and the presence of dyes highly influences water quality because most of them are considered to be toxic or even carcinogenic, posing a serious hazard to living organisms.[2,3] So, water pollution and contamination is one of the biggest and the most alarming problems which demands formidable and effective solutions. The situation is worrisome particularly in developing countries and the nonavailability of economical water treatment techniques further aggravates the situation.[4,5]

Many technologies such as chemical oxidation, photochemical degradation, ultrasonic degradation, reverse osmosis, otation and adsorption procedures, and the like have been proposed for dye removal.[6–12] Nevertheless, adsorption is recognized as one of effective and economic method because of its high efficiency, low costs and easy operation.[13–17]Among various available adsorbents, semiconductors have potential applications in water treatment in recent years owing to their high surface area and low production and regeneration costs.[18-20]Semiconductor photocatalysis has drawn ever-increasing worldwide interest because it is considered as cost-effective, sustainable and the most promising green chemical technology for dye removal. However, the rapid recombination of photogenerated charge carriers for single semiconductor has seriously inhibited photocatalytic performance. Interestingly, coupling two or more kinds of photocatalysts to form heterojunction can obviously enhance photocatalytic activity due to the effective charge separation.[21-28]

In general, a semiconductor with good photocatalytic activity may not have good adsorptive performance, and vice versa. Recently, in order to combine with the advantages of photocatalysis and adsorption technology, some researchers synthesized micro/nanomaterials possessing photocatalytic and adsorptive performance as well.[29-32] Upadhyay et al.[32] reviewed the role of graphene/metal oxide composites as photocatalysts, adsorbents and disinfectants in water treatment. However, the reported semiconductors couldn't simultaneously exhibit good adsorptive and photocatalytic performance.

As an important semiconductor, $Bi_2O_2CO_3$ belongs to the layered Aurivillius-related oxide family, comprising alternate $(Bi_2O_2)^{2+}$ and CO_3^{2-} layers. It has attracted great attentions due to their anisotropic crystal structure and internal static electric field effect, which favors the photo-induced charge separation and transfer. Coupling $Bi_2O_2CO_3$ with other semiconductors including Bi_2MoO_6,[25] ZnO,[26] C_3N_4,[27] TiO_2[28]and $Bi_4O_5I_2$[24] has been clearly demonstrated to improve their photocatalytic

[a]The Key Laboratory of Functional Molecular Solids, Ministry of Education, College of Chemistry and Materials Science, Anhui Normal University, Wuhu 241000, ChinaFax: (+86) 551-6360 2346; E-mail: kimipeng@mail.ahnu.edu.cn
[b]Division of Nanomaterials and Chemistry, Hefei National Laboratory for Physical Sciences at Microscale, Department of Chemistry, University of Science and Technology of China, Hefei 230026, P. R China.
† Electronic Supplementary Information (ESI) available: [details of any supplementary information available should be included here]. See http://dx.doi.org/10.1039/b000000x/

activities due to the formation of heterojunctions which can significantly reduce the recombination and speed up the separation rate of photogenerated charge carriers. However, $Bi_2O_2CO_3$ heterojunctions not only with high adsorptive capability, but also with high photocatalytic activity have not been reported at present.

In this paper, we successfully synthesized one-dimensional $Bi_2O_2CO_3$-$Bi(OHC_2O_4)$•$2H_2O$ heterostructure with both high adsorptive capability and excellent photocatalytic performance. It could adsorb 95.78 mg/g of MO dye, and degrade high concentration organic dyes in short time under the solar/UV light irradiation. This outstanding adsorptive and photocatalytic performance is due to two reasons: 1) large BET surface area; 2) the formation of a large number of junctions in $Bi_2O_2CO_3$-$Bi(OHC_2O_4)$•$2H_2O$ heterostructure. The trapping experiment of active species during the photocatalytic degradation proved that $O_2^{-\bullet}$ radical and h^+ were the main active species. The possible photocatalytic mechanism of $Bi_2O_2CO_3$-$Bi(OHC_2O_4)$•$2H_2O$ heterostructure was discussed in detail.

Experimental Section

Sample Preparation

All reagents were analytical grade and used without any further purification in our experiment.

The $Bi(OHC_2O_4)$•$2H_2O$ nanorods were prepared through a hydrothermal process according to our previous report.[22] 6 mmol of $Bi(NO_3)_3$•$5H_2O$ and 9 mmol of $Na_2C_2O_4$ were added separately in distilled water (20 mL) to obtain solution A and B. Subsequently, the solution B was added dropwise into A. The mixtures were stirred for 30 min at room temperature in air, then added into a Teflon-liner stainless steel autoclave and maintained at 120 ºC for 40 h. The samples were washed several times with anhydrous ethanol and distilled water, and then dried in air at 60 ºC for 6 h.

Then, $Bi_2O_2CO_3$-$Bi(OHC_2O_4)$•$2H_2O$ samples were prepared through a stirring process. In a typical experiment, $Bi(OHC_2O_4)$•$2H_2O$ nanorods (0.5 mmol), CTAB (0.5 g) and different amounts of Na_2CO_3 were dispersed into distilled water (40 mL) under magnetic stirring for 30 min, and then different amounts of $Bi(NO_3)_3$•$5H_2O$ was added with constant stirring for 2 h to obtained samples. The products were washed with distilled water and anhydrous ethanol, and then dried in air at 60 ºC for 4 h. The as-obtained products with the molar ratio of $Bi(OHC_2O_4)$•$2H_2O$:$Bi(NO_3)_3$•$5H_2O$ 20:1, 20:2, 20:3 and 20:5, were noted as S1, S2, S3 and S4, respectively.

Test of Photocatalytic Activity

Photocatalytic performance of the obtained samples was evaluated by the degradation of dyes under solar light irradiation. The optical system used for the photocatalytic reaction consisted of a 500 W Xe lamp (PLS-SXE300/300UV, Trusttech Co., Ltd. Beijing) and a 400 nm cutoff filter. In each experiment, 100 mg of sample was dispersed in 100 mL of dye under vigorous stirring for 30 min in the dark to reach an adsorption-desorption equilibrium between the photocatalyst and dye before light irradiation. Then, the suspension was illuminated by the Xe lamp under magnetic stirring. At irradiation time intervals, 4 mL of suspension was collected, and centrifuged to remove the photocatalyst. The solution was analyzed by UV-Vis absorption spectra. Additionally, the recycle experiments were performed for ten consecutive cycles to test the durability. After each cycle, the catalyst was centrifuged and used directly for the next test.

Adsorption experiments

To determine the adsorption capacities of different samples, the obtained samples were as adsorbents for MO removal. The 100 mg of samples were added to 100 mL MO solutions with initial concentrations from 50 mg/L to 105 mg/L (5 mg/L intervals) until the equilibrium time was reached. The two phases were separated by centrifugation. The final MO concentrations remaining in the solution were measured by a UV-Vis spectrophotometer at 465 nm.

Adsorption kinetic experiments were conducted by adding 100 mg of adsorbents into a 100 mL solution at room temperature in air. The suspension was stirred in the dark for different time and above 4 mL of suspension was withdrawn, and centrifuged to remove the precipitate with UV-Vis absorption spectra.

The amount of adsorbed MO at equilibrium was calculated according to the following equations

$$q_e = (C_0 - C_e)\ V/M$$

where V is the volume of the aqueous solution (L), and M is the weight of the adsorbent (g), C_0 and C_t are the initial and final concentrations of MO in solutions, respectively.

Characterization

Field emission scanning electron microscopy (FE-SEM) images were recorded on a Hitachi S-4800 microscope. Transmission electron microscopic (TEM) images, high-resolution transmission electron microscopic (HRTEM) images and the selected area electron diffraction (SAED) patterns were performed on a JEOL-2010 microscope with an accelerating voltage of 200 kV. X-Ray powder diffraction (XRD) was carried out on a Rigaku (Japan) D/max -γA X-ray diffractometer with Cu-Kα radiation (λ = 0.154178 nm). UV-vis diffuse-reflectance spectrum was recorded with a UV-2450 spectrophotometer in the wavelength range of 200-800 nm at room temperature. $BaSO_4$ was used as the reflectance standard material. The X-Ray photoelectron spectroscopy (XPS) was performed on a Perkin-Elmer RBD upgraded PHI-5000C ESCA system. Nitrogen adsorption/desorption measurements were performed at 77 K using a Micromeritics Tristar II 3020 M analyzer after the samples were degassed at 180 ºC for 6 h. The Brunauer-Emmett-Teller (BET) surface area was estimated by using adsorption data in a relative pressure range from 0.05 to 0.3.

Results and discussion

X-ray powder diffraction (XRD) was used to identify the structure and phase composition. Fig. 1 shows the XRD patterns of the obtained $Bi_2O_2CO_3$-$Bi(OHC_2O_4)$•$2H_2O$ heterojunctions with different loaded-$Bi_2O_2CO_3$ contents and pure $Bi(OHC_2O_4)$•$2H_2O$ nanorods. It can be seen that all the diffraction peaks of bismuth oxalate ($Bi(OHC_2O_4)$•$2H_2O$) is the same with previous report.[22] With the increase of the loaded-$Bi_2O_2CO_3$ content, the new diffraction peaks appear and their intensities increase gradually (S1 → S3 samples), which are ascribed to the orthorhombic phase of $Bi_2O_2CO_3$ (JCPDS No.

41-1488). When the loaded-$Bi_2O_2CO_3$ content is very high (S4 sample), only the peaks of $Bi_2O_2CO_3$ can be found and those of $Bi(OHC_2O_4)•2H_2O$ nanorods disappear completely. So, it is concluded that S4 sample is pure $Bi_2O_2CO_3$.

The SEM image of the $Bi(OHC_2O_4)•2H_2O$ precursor was shown in Fig.S1. It can be seen that $Bi(OHC_2O_4)•2H_2O$ precursor is rod-like structure, with the average diameter of 450 nm and length of 5.5 μm, respectively. Fig. 2 displayed the SEM images of the obtained $Bi_2O_2CO_3$-$Bi(OHC_2O_4)•2H_2O$ heterojunctions and pure $Bi_2O_2CO_3$. The $Bi_2O_2CO_3$-$Bi(OHC_2O_4)•2H_2O$ junctions are also rod-like structures, and ultrathin $Bi_2O_2CO_3$ nanosheets grow vertically onto the surface of $Bi(OHC_2O_4)•2H_2O$ nanorod (Fig. 2a). Meanwhile, the more of the loaded-$Bi_2O_2CO_3$ content, the more ultrathin $Bi_2O_2CO_3$ nanosheets grow orderly onto the $Bi(OHC_2O_4)•2H_2O$ rods along the long axial direction (Fig. 2b, c). The gap between $Bi_2O_2CO_3$ nanosheets becomes narrower and narrower, and the $Bi(OHC_2O_4)•2H_2O$ rod becomes thinner and thinner. Finally $Bi(OHC_2O_4)•2H_2O$ rod completely disappear, and pure $Bi_2O_2CO_3$ is formed due to the Kirkendall effect (Fig.2d).[33] However, the one-dimensional $Bi_2O_2CO_3$ structure collapses due to the disappearance of the $Bi(OHC_2O_4)•2H_2O$ skeleton, and forms short rods constituted of many nanosheets (Fig. 1d). This result implies that the BET surface area of $Bi_2O_2CO_3$ will be larger than that of $Bi_2O_2CO_3$-$Bi(OHC_2O_4)•2H_2O$ heterojunctions, which can be proved by the following result of BET surface area (Table 1).

To further obtain information about the structure of the sample, the S2 heterojunction was characterized by transmission electron microscopy (TEM). As shown in Fig. 3a, it can be clearly seen that the $Bi_2O_2CO_3$ nanosheets vertically grow onto the surface of the $Bi(OHC_2O_4)•2H_2O$ rod, which is consistent with the result of the SEM measurements. Fig. 3b shows the high-resolution transmission electron microscopic (HRTEM) image taken from the tip (red square highlighted in Fig. 3a) of the $Bi_2O_2CO_3$ nanosheet. It is found that the lattice fringe (the edge of nanosheet) with interplanar spacing of 0.684 nm corresponds well to (002), while the fringe spacing of 0.273 nm corresponds to (110) crystallographic planes of tetragonal $Bi_2O_2CO_3$.

XPS measurement was also performed to further confirm the formation of $Bi_2O_2CO_3$-$Bi(OHC_2O_4)•2H_2O$ heterostructures and investigate the chemical state of elements in this heterostructure. Fig. 4a shows the full XPS spectra of the as-prepared S2, $Bi_2O_2CO_3$ and $Bi(OHC_2O_4)•2H_2O$ samples, demonstrating that all the products were mainly composed of Bi, C and O elements. In the high resolution Bi 4f XPS spectrum of $Bi_2O_2CO_3$ (Fig. 3b), The peaks located at 164.1 and 158.8 eV are attributed to Bi $4f_{5/2}$ and Bi $4f_{7/2}$, respectively, which proves Bi ions in $Bi_2O_2CO_3$ sample are in form of Bi^{3+}.[21, 22] More importantly, in the high-resolution Bi 4f XPS spectrum of S2, the peaks of Bi 4f shift to higher binding energies due to the strong interaction between $Bi_2O_2CO_3$ and $Bi(OHC_2O_4)•2H_2O$ phases. A similar phenomenon was also observed in the C 1s spectra of $Bi_2O_2CO_3$-$Bi(OHC_2O_4)•2H_2O$ sample (Fig.4c). In addition, the location and relative intensity of the Bi–O (530.2 eV) and Bi–O (531.0 eV) peaks in S2 display obvious differences from those of $Bi(OHC_2O_4)•2H_2O$ and $Bi_2O_2CO_3$ (Fig. 4d), indicating that the formation of a heterojunction significantly influenced the environment of a chemical bond in the crystal.

Fig. S2a displays the nitrogen adsorption–desorption isotherms of the obtained samples. The shape of the isotherm is a type IV isotherm with a type H3 hysteresis loop at high relative pressures according to the IUPAC classification, which indicates that these samples are mesoporous structures in the pore diameter range of 2−50 nm.[35] This result can be further confirmed by the corresponding pore size distribution, as shown in Fig. S2b. Table 1 gives the BET surface area of different samples. It can be found that the pure $Bi_2O_2CO_3$ nanosheet has the largest BET specific surface areas (26.478 $m^2•g^{-1}$) which is consistent with the result of SEM image (Fig. 2 d), and $Bi(OHC_2O_4)•2H_2O$ nanorod has the smallest BET surface area (3.844 $m^2•g^{-1}$). The BET surface area of $Bi_2O_2CO_3$-$Bi(OHC_2O_4)•2H_2O$ heterojunctions increase gradually from S1(8.782 $m^2•g^{-1}$) to S3 (14.227 $m^2•g^{-1}$).

The optical absorption property of the semiconductor is one of the important factors determining its photocatalytic performance. Fig. 5 (a) displays the diffuse reflectance spectroscopy (DRS) of the obtained samples at room temperature. The absorption edge of all samples is <400 nm, which shows they only absorb UV light. The optical band gap of $Bi(OHC_2O_4)•2H_2O$ and $Bi_2O_2CO_3$ can be determined by the following equation:[36]

$$\alpha h\nu = A(h\nu - Eg)^{2/n}$$

in which α, h, ν, A and Eg are the absorption coefficient, Planck constant, light frequency, a constant and band gap, respectively. And n equals to 4 for indirect band gap and 1 for direct band gap. here n = 1 for $Bi(OHC_2O_4)•2H_2O$ and n = 4 for $Bi_2O_2CO_3$. In Fig. 5b, the extrapolation of the $(\alpha h\nu)^{n/2}$ against hν plot on the x intercepts gives the optical band gap of 3.92 eV for $Bi(OHC_2O_4)•2H_2O$ and 3.32 eV for $Bi_2O_2CO_3$.

The photocatalytic activity of S1, S2, S3, $Bi_2O_2CO_3$ and $Bi(OHC_2O_4)•2H_2O$ samples were evaluated by degradation of RhB (20 mg/L) dye in aqueous solution under solar light (containing 4% UV light) irradiation. As shown in Fig. 6a, S2 sample displays the highest photocatalytic activity among all the photocatlaysts, and RhB molecules can be completely decolored in 30 min under solar light irradiation. The UV-vis absorbance spectra of RhB using different samples as photocatalysts are shown in Fig. S3. Fig. 6(b) displays the linear relationship between $-\ln(C/C_0)$ and irradiation time, suggesting that the photocatalytic degradation reaction of RhB over the as-prepared catalysts should belong to the first-order kinetic relation. The calculated reaction rates have been shown in Table 1. The reaction rate constant of 0.148 min^{-1} for S2 sample is as 200, which is twice as ones for $Bi(OHC_2O_4)•2H_2O$ and $Bi_2O_2CO_3$. Compared with Bi_2O_3-Bi_2WO_6,[22] BiOI/$Bi_4O_5I_2$/$Bi_2O_2CO_3$ heterojunction,[24] and $BiPO_4$/$Bi_2O_2CO_3$ heterostructure,[37] $Bi_2O_2CO_3$-$Bi(OHC_2O_4)•2H_2O$ heterojunction exhibits outstanding photocatalytic performance, which is ascribed to the formation of enough junctions in the S2 sample. According to the SEM images (Fig. 2) of $Bi_2O_2CO_3$-$Bi(OHC_2O_4)•2H_2O$ heterojunctions, for low $Bi_2O_2CO_3$ content in S1 sample, sparse $Bi_2O_2CO_3$ nanosheets grown on

$Bi(OHC_2O_4)•2H_2O$ rods are observed, so only a small number of junctions are generated, leading to a low photocatalytic activity. When the $Bi_2O_2CO_3$ content is increased in the S2 sample, a large number of junctions are formed, thus resulting in the highest photocatalytic activity for the optimal S2 sample. With the $Bi_2O_2CO_3$ content further increasing, dense $Bi_2O_2CO_3$ nanosheets almost cover the $Bi(OHC_2O_4)•2H_2O$ rods, as observed in S3 sample (Fig. 2c), which decreases the light irradiation on $Bi(OHC_2O_4)•2H_2O$ rods and the junction interfaces. This shielding effect of dense $Bi_2O_2CO_3$ nanosheets coating on the $Bi(OHC_2O_4)•2H_2O$ rods makes the photocatalytic activity of S3 sample decrease.

Under UV light irradiation, S2 heterojunction shows better photocatalytic activity to degrade high concentrations of MB, RhB and MO. 20 mg/L of RhB molecules, 30 mg/L of MB and 75 of mg/L of MO can be completely decolored in 15, 25 and 120 min, respectively (Fig.6c), which can be proved by the photographies of S2 after UV light irradiation (Fig. 6d).

From Fig. 6a, we also find that the mixture sample (the mole ratio of $Bi(OHC_2O_4)•2H_2O$ and $Bi_2O_2CO_3$ in the mixture is equal to that in the S2 heterostructure) shows low photocatalytic activity to degrade RhB under solar light irradiation. It is proved that the formation of junctions is very important to enhance photocatalytic performance of material. Moreover, even though $Bi_2O_2CO_3$ nanosheets have larger BET surface area than S2 sample, its reaction rate constant k is obviously smaller than S2's, which further proves that junctions is a more important factor than BET surface area to improve photocatalytic activity of the sample under solar light irradiation.

To investigate the stability of photocatalytic performance in solar light region, the S2 sample was used to degrade RhB (20 mg/L) dye in ten repeated cycles, and the results were shown in Fig. S4. It is noteworthy that S2 photocatalyst exhibits good photostability under solar light irradiation (Fig. S4a), and its photocatalytic efficiency reduces 2% after ten repeated cycles. From the XRD pattern (Fig. S4b), it can be found that the crystal phase of S2 sample is still $Bi_2O_2CO_3$-$Bi(OHC_2O_4)•2H_2O$ heterojunctions, demonstrating its high stability in the process of photocatalysis.

In order to explore the photocatalytic mechanism of $Bi_2O_2CO_3$-$Bi(OHC_2O_4)•2H_2O$ heterojunctions in detail, the trapping experiments of active species during this photocatalytic process were carried out. Benzoquinone (BQ), tertbutyl alcohol (TBA), and ammonium oxalate (AO) were used as scavengers of superoxide radical ($•O_2^-$), hydroxyl radical (•OH) and hole (h^+), respectively.[38,21] Fig. 7 shows the effect of different scavengers on the photodegradation rate over the S2 sample. It can be found that the addition of TBA does not cause significant deactivation of S2 photocatalyst. However, the photocatalytic performance of S2 significantly decreases by the addition of BQ or AO. These results suggest that $•O_2^-$ and h^+ are the main active species in the photocatalytic process under solar light irradiation.

To determine the relative positions of conduction band (CB) and VB edges, the total densities of states of VB for $Bi(OHC_2O_4)•2H_2O$ and $Bi_2O_2CO_3$ were measured, as shown in Fig. 8. The VB edges of $Bi(OHC_2O_4)•2H_2O$ and $Bi_2O_2CO_3$ are 2.55 and 1.66 eV, respectively. According to the VB edges, combining with band gap of $Bi(OHC_2O_4)•2H_2O$ (3.92 eV) and $Bi_2O_2CO_3$ (3.32 eV), the CB edge potential of $Bi(OHC_2O_4)•2H_2O$ and $Bi_2O_2CO_3$ is −1.37 and −1.66 eV, respectively, calculated from the equation of $E_{CB} = E_{VB} − Eg$.

Based on the above results and analysis, the degradation mechanism of $Bi_2O_2CO_3$-$Bi(OHC_2O_4)•2H_2O$ heterostructures under solar light irradiation was illustrated in Fig. 9. When $Bi_2O_2CO_3$ and $Bi(OHC_2O_4)•2H_2O$ semiconductors are in contact to form $Bi_2O_2CO_3$-$Bi(OHC_2O_4)•2H_2O$ heterojunction, the excited electrons in the conduction band (CB) of $Bi_2O_2CO_3$ can transfer to CB of $Bi(OHC_2O_4)•2H_2O$ due to their different conduct band position, while the holes remain in the valence band (VB) of $Bi_2O_2CO_3$. Meanwhile, the photogenerated holes on the VB of $Bi(OHC_2O_4)•2H_2O$ transfer to that of $Bi_2O_2CO_3$ due to different VB position, but the excited electrons stay in the CB of $Bi(OHC_2O_4)•2H_2O$. Thus, the photogenerated electron-hole pairs in $Bi(OHC_2O_4)•2H_2O$-$Bi_2O_2CO_3$ heterostructure can be effectively separated and then the photocatalytic activity is significantly enhanced due to the formation of $Bi_2O_2CO_3$-$Bi(OHC_2O_4)•2H_2O$ heterojunctions.

According to Fig. 9, it can be seen that the CB potential (-1.37 eV) of $Bi(OHC_2O_4)•2H_2O$ is enough negative to $E^0(O_2/•O_2−)$ (-0.046 eV vs NHE), the electrons in the CB of $Bi(OHC_2O_4)•2H_2O$ can reduce O_2 adsorbed on the surface of $Bi(OHC_2O_4)•2H_2O$ nanorods to $•O_2^-$ through one electron reducing reaction. The oxidation potential of $Bi_2O_2CO_3$ is 1.66 eV, which indicates that the photogenerated holes cannot directly oxidize hydroxyl groups or water molecules adsorbed on the surface of $Bi_2O_2CO_3$ to generate •OH radicals (2.7 V vs NHE). Hence, the h^+ and $•O_2^-$ radicals rather than •OH are the main active species and react directly with RhB in the solution for efficient degradation.

As we know, the LUMO RhB (+0.95 V vs NHE) is excited to RhB* (−1.42 V vs NHE) [39] when irradiated by visible light, then RhB* injects electrons into the CB of semiconductor, and subsequently the photocatalytic process occurs on the surface of semiconductor. Apparently, the CB potential of $Bi_2O_2CO_3$ is much more positive than the LUMO potential of the RhB molecule (see Fig. 8). As a result, the electron injection from the excited RhB molecules into the CB of $Bi_2O_2CO_3$ could not be favoured. This can explain why the RhB dye only can be adsorbed, but not be degraded by pure $Bi_2O_2CO_3$ sample in the visible light irradiation (Fig. S5). However, when $Bi_2O_2CO_3$-$Bi(OHC_2O_4)•2H_2O$ heterostructure was used as photocatalyst, the photogenerated electrons of RhB molecules can effectively inject into the CB of $Bi(OHC_2O_4)•2H_2O$ because their LUMO potentials (-1.42V vs NHE) is more negative than the CB potential of $Bi(OHC_2O_4)•2H_2O$ (-1.37eV). Simultaneously, RhB is efficiently degraded.

The obtained heterojunctions and pure $Bi_2O_2CO_3$ not only show superior photocatalytic activity, but also display excellent absorptive ability. Fig. S6 displays their absorptive activity to RhB (20 mg/L), MB (20 mg/L) and MO (20 mg/L) dyes. It can be found that all the $Bi_2O_2CO_3$-$Bi(OHC_2O_4)•2H_2O$ heterostructures and $Bi_2O_2CO_3$ display high adsorptive capability and selectivity to MO dye. Further adsorption experiments were carried out. As shown in Fig. 10, MO (75 mg/L) dye in aqueous solution was used to evaluate the absorptive ability of S1, S2, S3 and $Bi_2O_2CO_3$ samples. It can be seen that S3 sample displays the highest adsorptive capability among four samples. It is noteworthy that all samples can quickly reach an adsorption/desorption equilibrium within 5 min. As we know, BET surface area plays

an important role in material's adsorptive capability. Generally, the larger BET surface area is, the stronger the adsorptive ability is. According to Table 1, BET surface area of heterostructures gradually increases from S1 to S3 and their adsorptive abilities also enhance in order. However, $Bi_2O_2CO_3$ owns the largest BET area in all the obtained samples, but its adsorptive ability is obviously weaker than that of S3 and S2. The above result implies that there exists other reason to affect the adsorptive ability of materials except BET surface area. Compare with their differences in detail, we can find that S3 and S2 are heterojunctions and $Bi_2O_2CO_3$ is single material. So, the enhanced adsorptive ability of S3 and S2 is attributed to the synergistic effect of the formation of numbers of junctions and large BET surface area.

The adsorption of MO on S3 follows the langmuir isotherm (Fig. S7) because of the high correlation coefficients (R^2 = 0.998). The maximum adsorption capacity (q_m) of the adsorbent S3 can be obtained from the intercept of the line of Ce/qe against Ce, and the q_m is 95.78 mg/g.

Previously some researchers investigated several adsorbents for the removal of MO from aqueous solutions.[40-53] A comparison of the contact time and the adsorption capacities of MO onto various adsorbents is shown in Table 2, which clearly suggests that although the $Bi_2O_2CO_3$-$Bi(OHC_2O_4)$•$2H_2O$ heterojunctions have a relatively suitable adsorption, they hold much greater potential for water treatment due to the short contact time.

A good adsorbent should not only be quick in adsorption of pollutants but also should exhibit speedy and complete desorption of pollutants during regeneration in order to be reused. For organic pollutants, such as dyes and pesticides, regeneration can be carried out by simply washing composite with a solvent to dissolve away the pollutants. The S3 heterojunction not only shows remarkable adsorptive ability for MO, but also displays good repeatability. When S3 sample adsorbed MO dye was dispersed into ethanol solution, MO dye molecules can desorb completely from S3 (Fig. S8), and S3 can be reused many times. Fig. 11 shows the adsorption capacities of the regenerated S3 adsorbent. It can be found S3 sample displays good adsorptive ability for MO (80 mg/L), and its adsorptive efficiency only reduces 2% after eight repeated cycles, which also can be proved by the photograph of MO solution after eighth adsorption (inset in Fig.11).

Conclusions

In summary, the novel one-dimensional $Bi(OHC_2O_4)$•$2H_2O$-$Bi_2O_2CO_3$ heterostructures with both excellent adsorptive and photocatalytic performance have been prepared for the first time. $Bi_2O_2CO_3$ nanosheets uniformly grew on the surface of the $Bi(OHC_2O_4)$•$2H_2O$ nanorods along axial orientation. The obtained $Bi_2O_2CO_3$-$Bi(OHC_2O_4)$•$2H_2O$ heterojunctions exhibit excellent photocatalytic activity to degrade organic dyes under solar/UV light irradiation. High concentration RhB (20 mg/L), MB (30 mg/L) and MO (75 mg/L) dyes can be completely degraded in 15, 25 and 120 min, respectively, under UV light irradiation using S2 sample as photocatalyst. The reaction rate constant of 0.148 min^{-1} for S2 is as 200 and 2 times as ones for $Bi(OHC_2O_4)$•$2H_2O$ and $Bi_2O_2CO_3$ under solar light irradiation. $Bi_2O_2CO_3$-$Bi(OHC_2O_4)$•$2H_2O$ heterostructure also shows excellent adsorption performance. Its adsorptive capacity reaches 95.78 mg/g for MO, with contact time of only 5 min. According to the investigation, these outstanding adsorptive and photocatlytic performance are ascribed to the synergistic effect of big BET surface area and the formed junctions in $Bi_2O_2CO_3$-$Bi(OHC_2O_4)$•$2H_2O$ heterostructure. Generally, this study provides a general and effective method to fabricate unique 1D $Bi_2O_2CO_3$-$Bi(OHC_2O_4)$•$2H_2O$ heterostructure with both photocatalytic and adsorptive performance on a large scale.

Acknowledgements

This work is supported by the National Natural Science Foundation of China (21101006).

Notes and references

‡ Additional figures are given in supporting information.

1 X. Liu, L. Yan, W. Yin, L. Zhou, G. Tian, J. Shi, Z. Yang, D. Xiao, Z. Gu and Y. Zhao, *J. Mater. Chem. A*, 2014, **2**, 12296–12303.
2 M. A. M. Salleh, D. K. Mahmoud, W. A. W. A. Karim and A. Idris, *Desalination*, 2011, **280**, 1–13.
3 V. K. Gupta, R. Kumar, A. Nayak, T. A. Saleh and M. A. Barakat, *Adv. Colloid Interface Sci.*, 2013, **193–194**, 24–34.
4 R. Haberl, Water Sci. *Technol*., 1999, **40**, 11–17.
5 H. Bouwer, *Water Sci. Technol*.., 2000, 45, 217–228.
6 L. Zhang, H. Li, Y. Liu, Z. Tian, B. Yang, Z. Sun and S. Yan, *RSC Adv*., 2014, **4**, 48703–48711.
7 J. Qu, L. Shi, C. He, F. Gao, B. Li, Q. Zhou, H. Hu, G. Shao, X. Wang and J. Qiu, *Carbon*, 2014, **66**, 485–492.
8 Y. Liu, G. Cui, C. Luo, L. Zhang, Y. Guo and S. Yan, *RSC Adv*., 2014, **4**, 55162–55172.
9 H. Zhao, G. Zhang and Q. Zhang, *Ultrason. Sonochem*., 2014, **2**1, 991–996.
10 V. K. Gupta, R. Jain, A. Mittal, T. A. Saleh, A. Nayak, S. Agarwal and S. Sikarwar, *Mater. Sci. Eng*., C, 2012, **32**, 12–17.
11 T. A. Saleh and V. K. Gupta, *J. Colloid Interface Sci*., 2012, **371**, 101–106.
12 T. A. Saleh and V. K. Gupta, *J. Colloid Interface Sci.*, 2011, **362**, 337–344.
13 Y. Haldorai and J. J. Shim, *Appl. Surf. Sci.*, 2014, **292**, 447–453.
14 V. K. Gupta and T. A. Saleh, Environ. *Sci. Pollut. Res. Int*., 2013, **20**, 2828–2843.
15 Z. Tian, B. Yang, G. Cui, L. Zhang, Y. Guo and S. Yan, *RSC Adv*., 2015, **5**, 2266–2275.
16 V. K. Gupta, S. Agarwal and T. A. Saleh, *J. Hazard. Mater.,* 2011, **185**, 17–23.
17 Y. Y. Xu, M. Zhou, H. J. Geng, J. J. Hao, Q. Q. Ou, S. D. Qi, H. L. Chen and X. G. Chen, *Appl. Surf. Sci*., 2012, **258**, 3897–3902.
18 V. K. Gupta, S. Agarwal and T. A. *Saleh, Water Res*., 2011, **45**, 2207–2212.
19 T. A. Saleh and V. K. Gupta, *Environ. Sci. Pollut. Res. Int*., 2012, **19**, 1224–1228.
20 Y. Liu, C. Luo, J. Sun, H. Z. Li, Z. Sun and S. Q. Yan, *J. Mater. Chem. A,* 2015, **3**, 5674–5682.
21 Y. Peng, Q. G. Chen, D. Wang, H. Y. Zhou and A. W. Xu, *CrystEngComm,* 2015, **17**, 569–576.
22 Y. Peng, M. Yan, Q. G. Chen, C. M. Fang, H. Y. Zhou and A. W. Xu, *J. Mater. Chem. A*, 2014, **2**, 8517-8524.
23 Y. Peng, P. P. Yu, Q. G. Chen, H. Y. Zhou and A. W. Xu, *J. Phys. Chem. C*, 2015, **119**, 13032-13040.
24 Y. Peng, P. P. Yu, H. Y. Zhou and A. W. Xu, *New J. Chem*., 2015, **39**, 8321-8328.
25 Y. S. Xu and W. D. Zhang, *Appl. Catal. B: Environ.,* 2013, **140–141**, 306–316.

26 S. S. Xiao, Y. Q. Li , J. J. Hu, H. Li , X. P. Zhang, L. Liu and J. S. Lian, *CrystEngComm*, 2015, **17**, 3809-3819.
27 M. Xiong, L. Chen, Q. Yuan, S. L. Luo, C. T. Au and S. F. Yin, *Dalton Trans.*, 2014, **43**, 8331–8337.
28 Y. H. Ao, L. Y. Xu, P. F. Wang, C. Wang, J. Hou, J. Qian and Y. Li, *Appl. Surf. Sci.,* 2015, **355**, 411-418.
29 C. W. Tan, G. Q. Zhu, M. Hojamberdiev, K. S. Lokesh, X. C. Luo, L. Jin, J.P. Zhou, P. Liu, *J. Hazard. Mater.*, 2014, **278**, 572–583.
30 Y. Park, Y. Na, D. Pradhan, B. K. Min and Y. Sohn, *CrystEngComm*, 2014, **16**, 3155–3167.
31 T. Madrakian, A. Afkhami, R. Haryani and M. Ahmadi, *RSC Adv*., 2014, **4**, 44841−44847.
32 R. K. Upadhyay, N. Soin and S. S. Roy, *RSC Adv*., 2014, **4**, 3823–3851.
33 W. S. Wang, M. Dahl and Y. D. Yin, *Chem. Mater.*, 2013, **25**, 1179−1189.
34 K. S. W. Sing, D. H. Everett, R. A. W. Haul, L. Moscou, R. A. Pierotti, J. Rouquerol and T. Siemieniewska, *Pure. Appl. Chem.,* 1985, **57**, 603–619.
35 G. I. N. Waterhouse, G. A. Bowmaker and J. B. Metson, *Phys. Chem. Chem. Phys.*, 2001, **3**, 3838–3845.
36 M. A. Butler, *J. Appl. Phys.*, 1977, **48**, 1914−1920.
37 Y. M. Liu, P. Zhang, H. Lv, J. Guang, S. Li and J. H. Jiang, *Rsc Adv.*, 2015, **5**(102), 83764−83772.
38 G. V. Buxton, C. L. Greenstock, W. P. Helman and A. B. Ross, *J. Phys. Chem. Ref. Data.,* 1988, **17**, 513–886.
39 T. Shen, Z. G. Zhao, Q.Yu and H. J. Xu, *J. Photochem. Photobiol. A*, 1989, **47**, 203−212.
40 J. Ma, F. Yu, L. Zhou, L. Jin, M. Yang, J. Luan, Y. Tang, H. Fan, Z. Yuan and J. Chen, *ACS Appl. Mater. Interf.*, 2012, **4**, 5749–5760.
41 Z. M. Ni, S. J. Xia, L. G. Wang, F. F. Xing and G. X. Pan, *J. Colloid Interface Sci.*, 2007, **316**, 284–291.
42 H. Chen, J. Zhao, J. Wu and G. Dai, *J. Hazard. Mater.*, 2011, **192**, 246–254.
43 J. H. Huang, K. L. Huang, S. Q. Liu, A. T. Wang and C. Yan, *Colloids Surf., A*, 2008, **330**, 55–61.
44 M. Arshadi, F. Salimi Vahid, J. W. L. Salvacion and M. Soleymanzadeh, *Appl. Surf. Sci.*, 2013, **280**, 726–736.
45 E. Haque, J. E. Lee, I. T. Jang, Y. K. Hwang, J. S. Chang, J. Jegal and S. H. Jhung, *J. Hazard. Mater.*, 2010, **181**, 535–542.
46 M. H. Do, N. H. Phan, T. D. Nguyen, T. T. Pham, V. K. Nguyen, T. T. Vu and T. K. Nguyen, *Chemosphere*, 2011, **85**, 1269–1276.
47 T. Kou, Y. Wang, C. Zhang, J. Sun and Z. Zhang, *Chem. Eng. J.*, 2013, **223**, 76–83.
48 X. Li, W. Xiao, G. He, W. Zheng, N. Yu and M. Tan, Colloids Surf. A, 2012, **408**, 79–86.49 Z. Jia, J. Liu, Q. Wang, M. Ye and R. Zhu, *Mater. Sci. Semicond. Process.,* 2014, **26**, 716–725.
50 Y. Yao, H. Bing, X. F. Fei and C. X. Feng, *Chem. Eng. J.*, 2011, **170**, 82–89.
51 H. Y. Zhu, R. Jiang, L. Xiao and G. M. Zeng, *Bioresour. Technol.*, 2010, **101**, 5063–5069.
52 Y. Liu, G. Cui, C. Luo, L. Zhang, Y. Guo and S. Yan, *RSC Adv*., 2014, **4**, 55162–55172.
53 Y. Liu, C. Luo, J. Sun, H. Z. Li, Z. B. Sun and S. Q. Yan, *J. Mater. Chem. A*, 2015, **3**, 5674–5682.

Fig. 1 The XRD patterns of $Bi(OHC_2O_4)•2H_2O$ nanorods, $Bi_2O_2CO_3$-$Bi(OHC_2O_4)•2H_2O$ heterojunctions and Standard Card of $Bi_2O_2CO_3$.

Fig. 2 FE-SEM images of (a) S1, (b) S2, (c) S3 and (d) S4($Bi_2O_2CO_3$).

Fig. 3 (a) The TEM and (b) HRTEM images of the S2 heterojunction.

Fig. 4 Survey (a) and high-resolution Bi 4f 3d (b), C 1s (c), and O 1s (d) XPS spectra of $Bi_2O_2CO_3$, $Bi(OHC_2O_4)•2H_2O$ and S2 samples.

Fig. 5 (a) UV-Vis diffuse reflectance spectra of $Bi(OHC_2O_4)•2H_2O$, $Bi_2O_2CO_3$ and $Bi_2O_2CO_3$-$Bi(OHC_2O_4)•2H_2O$ samples, (b) the plots of $(\alpha h\nu)^{2/n}$ vs. hν (n = 1 for $Bi(OHC_2O_4)•2H_2O$ and n = 4 for $Bi_2O_2CO_3$).

Fig. 6 (a) The degradation curves of RhB (20 mg/L) using different photocatalysts under solar light irradiation, (b) the linear relationship between $-\ln(C/C_0)$ and irradiation time; (c) the degradation curves of different dyes using S2 photocatalyst under UV light irradiation, and (d) the photographies of S2 after adsorption and UV light irradiation, respectively.

Fig. 7 Active species trapping experiments during the photocatalytic degradation to RhB (20mg/L) under solar light irradiation using S2 as photocatalyst.

Fig. 8 VB-XPS spectra of $Bi(OHC_2O_4)•2H_2O$ and $Bi_2O_2CO_3$.

Fig. 9 Schematic diagram of photocatalytic mechanism of $Bi_2O_2CO_3$-$Bi(OHC_2O_4)•2H_2O$ heterojunction.

Fig. 10 The absorption curve of MO (75 mg/L) using different samples as adsorbents. Inset in figure is photographs of MO solutions before and after absorption.

Fig. 11 Adsorption capacities of the S3 adsorbent after regeneration, (c_{MO} = 80 mg/L).

Table 1 The data of BET surface area, band gap, VB and CB, and pseudo-first-order rate constants for photodegradation of RhB over photocatalysts.

Table 2 Comparison of the adsorption capacities of MO onto various adsorbents

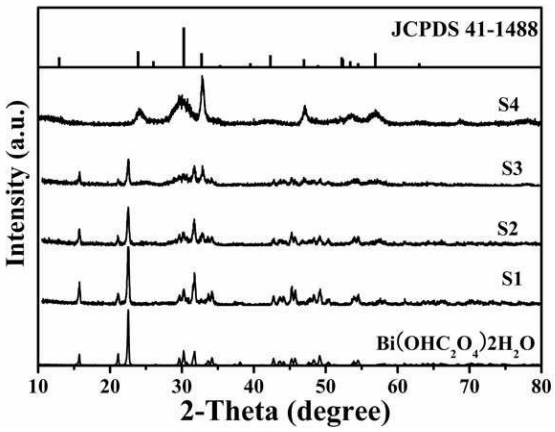

Fig.1

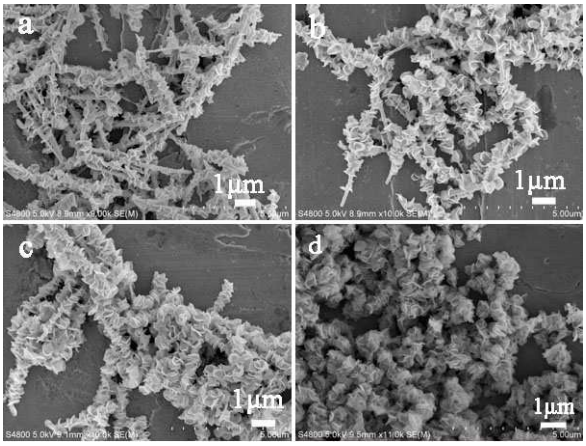

Fig.2

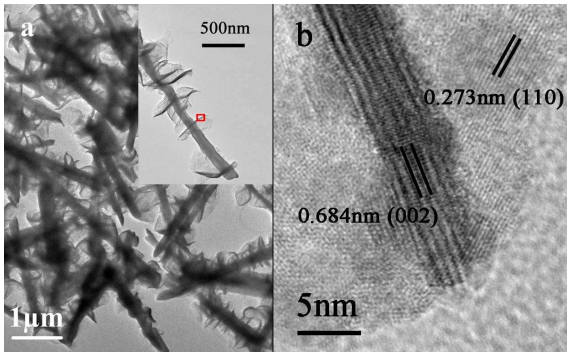

Fig.3

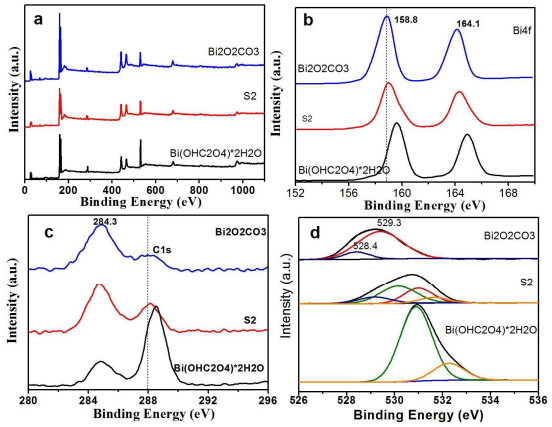

Fig.4

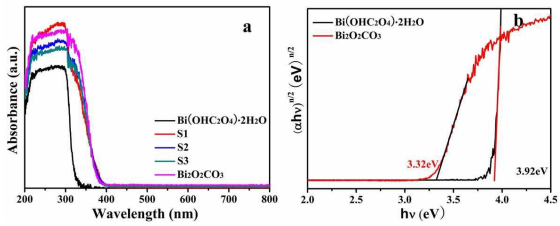

Fig.5

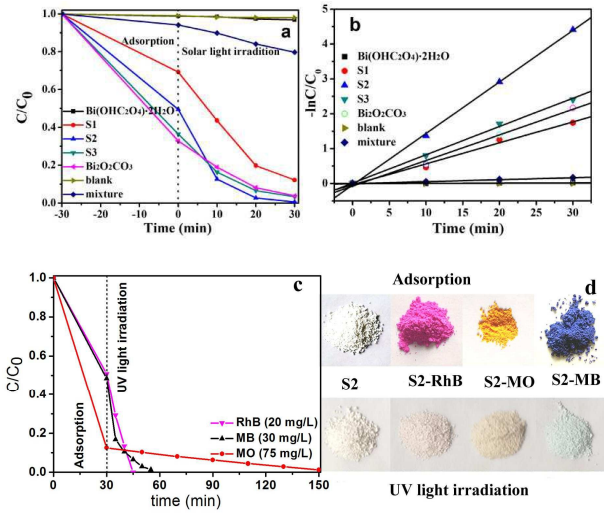

Fig.6

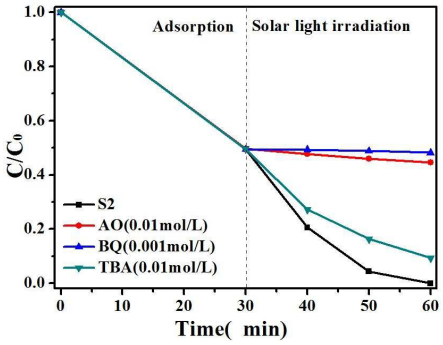

Fig.7

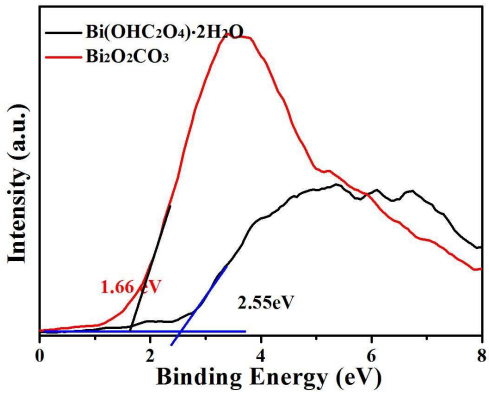

Fig.8

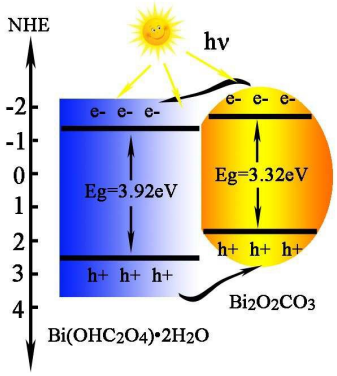

Fig.9

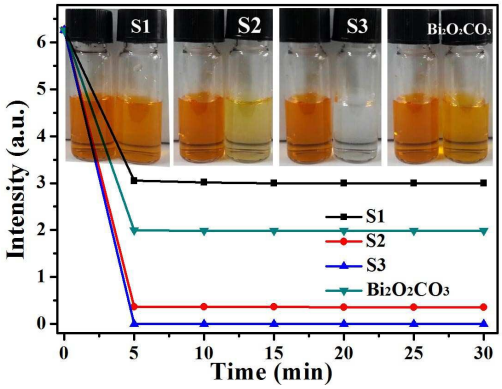

Fig.10

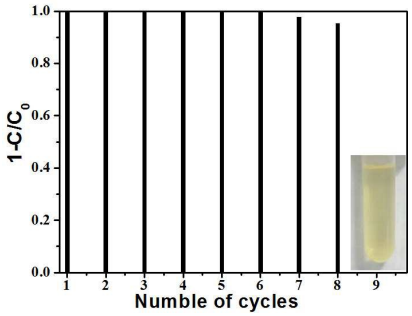

Fig.11

Table-1

samples	A_{BET} ($m^2 \cdot g^{-1}$)	VB (eV)	CB (eV)	Eg (eV)	k (min^{-1})
$Bi(OHC_2O_4)•2H_2O$	3.844	2.55	-1.37	3.92	0.00070
S1	8.782	/	/	/	0.06018
S2	10.560	/	/	/	0.14785
S3	14.227	/	/	/	0.08113
$Bi_2O_2CO_3$	26.487	1.66	-1.66	3.32	0.07340

Table 2

Adsorbents	Contanct time (min)	pH	q_{max} (mg/g^{-1})	Ref
Carbon nanotubes	45	Keep natural	52.86	50
Activated carbon	720	5.6	11.2	45
Chitosan/Fe_2O_3/CNTs	720	Keep nantural	60.09	51
Hypercrosslinked polymeric adsorbent	180	Keep nantural	70.9	43
Silkworm exuviae	720	7.0	87.03	42
$Bi_2O_2CO_3$-$Bi(OHC_2O_4)$•$2H_2O$ heterojunction	**5**	**6.8**	**95.78**	**our work**
K-δ-MnO_2 nanosheets	60	Keep natural	145	53
CNTs-A	180	7.0	149	40
Mesoporous NiO microspheres	60	7.0	164.7	49
NH2-MWCNTs	120	7.0	185.5	52
K-δ-MnO_2 nanoparticles	60	Keep natural	193	53
Calcined layered double hydroxides	120	6.0	200	41
Phragmites australis activated carbon	240	Keep natural	238.1	
Activated carbon/Fe_3O_4 nanoparticle composites	180	5.0	303.03	46
Core-shell Cu@Cu_2O	80	5.67	344.84	47
H-δ-MnO_2 nanosheets	60	Keep natural	357	53
SiO_2-Al_2O_3 mixed oxides	50	6.0	381	44
Mesoporous MgO nanoplates	120	Keep natural	370	48
Powdered activated carbon modified by HNO_3	180	5.0	384.62	46
H-δ-MnO_2 nanoparticles	60	Keep natural	427	53

A novel one-dimensional (1D) $Bi(OHC_2O_4)•2H_2O$-$Bi_2O_2CO_3$ heterostructures were synthesized by simple low temperature solution-phase method. The $Bi_2O_2CO_3$-$Bi(OHC_2O_4)•2H_2O$ heterostructure exhibits outstanding photocatalytic activity for degrading high concentration RhB, MB and MO dyes, and excellent adsorptive capability to MO dye.